Revue des Composites et des Matériaux Avancés-Journal of Composite and Advanced Materials
Vol. 34, No. 1, February, 2024, pp. 77-86
Journal homepage: http://iieta.org/journals/rcma

Fabrication and Mechanical Characterization of Functionally Graded NiTi/HA Alloys

Aseel M. Habeeb*, Nihad A. Salih

Department of Physics, College of Science, University of Babylon, Babel 51002, Iraq

Corresponding Author Email: sci.aseel.habeeb@uobabylon.edu.iq

https://doi.org/10.18280/rcma.340110

Received: 10 October 2023
Revised: 21 November 2023
Accepted: 22 December 2023
Available online: 29 February 2024

Keywords:
NiTi, HA, FGMs, particles size, compression, functionally graded

ABSTRACT

In the realm of biomaterials engineering, Functionally Graded Materials (FGMs) have emerged as a novel class of composites, characterized by spatial variations in composition that yield a gradient in properties tailor-made for specific applications. This investigation delineates the development of a multi-layered FGM composed of titanium, nickel, and hydroxyapatite (NiTi/HA), designed to address the challenges associated with bone implant integration. Porous NiTi, renowned for its mechanical compatibility with bone tissue, is coupled with hydroxyapatite, a material celebrated for its osteoconductive properties, to enhance bioactivity and promote bone ingrowth. The fabrication of this NiTi/HA FGM was realized through a powder metallurgy approach, culminating in the production of specimens with either three or five stratified layers that progressively transition from NiTi-rich at one extremity to HA-rich at the other. The compaction of these powders was executed under a pressure of 450 MPa, followed by a sintering process at 1000°C sustained for a duration of three hours—parameters meticulously chosen to optimize material integrity without compromising the functional gradient. Mechanical characterization was systematically conducted, revealing that the microhardness of the FGMs ranged from 269.6 to 458.11 kg/mm^2 and 365.5 to 436.5 kg/mm^2 for the three-layered and five-layered specimens, respectively. The density and porosity of these materials were also quantified, with the three-layered FGM (FGM_1) exhibiting an apparent density of 2.665 g/cm^3 and a porosity of 33.5%, while the five-layered FGM (FGM_2) displayed an increased density of 3.754 g/cm^3 and a reduced porosity of 24.6%. X-ray diffraction analysis verified the phase composition of the graded specimens, confirming the presence of the anticipated monoclinic NiTi, cubic NiTi, and hexagonal Ni_3Ti phases, integral to the material's function. The synergistic combination of the robust mechanical properties of the NiTi alloy with the superior bioactivity of hydroxyapatite underscores the potential of this FGM NiTi/HA for hard tissue implant applications, offering a promising avenue for the advancement of orthopedic treatments.

1. INTRODUCTION

The imperative for advanced bone grafting techniques in human medicine has been underscored by an escalating incidence of diseases and traumatic injuries. This has precipitated concerted efforts in the development of biological transplantation materials, pivotal in the restitution or substitution of human tissues, thereby augmenting their functional restoration [1]. Within this landscape, Functionally Graded Materials (FGMs) have emerged as composite materials, distinguished by a compositional gradient that linearly modulates their properties.

Historically, since the 1960s, titanium alloys have been the cornerstone of medical implants and biomaterials, lauded for their machinability, strength, and resistance to wear and corrosion [2, 3]. Yet, contemporary benchmarks in biomaterials demand more than mere mechanical robustness and biocompatibility; they necessitate materials that actively facilitate human tissue growth [3]. Titanium alloys, in their pure metallic state, fall short of these bioactivity requisites. Conversely, the Ni-Ti-based Nitinol alloy, characterized by equal atomic proportions of nickel and titanium, exhibits properties akin to shape-memory alloys (SMAs) and has garnered attention for its corrosion resistance.

Hydroxyapatite (HA), a calcium phosphate mineral with a hexagonal structure, embodies a white, natural substance utilized in the formation of bone and tooth enamel [4, 5]. The potential application of hydroxyapatite in material science and nanotechnology, particularly for medical purposes, is a subject of ongoing investigation. Hydroxyapatite's bioactivity is renowned; it is one of the few synthetic materials capable of fostering the growth of bone and teeth [6, 7]. Despite its biological compatibility, which mirrors that of human bone, HA is impeded by inadequate mechanical properties, curtailing its standalone application [8, 9].

The quest for innovative biomaterials, capable of achieving stable osseointegration, has become a focal point of research. Fusing the bioactivity of HA with the mechanical prowess of

metals is posited as a promising avenue for synthesizing desirable biomedical composites for load-bearing applications. Such composites have attained a balance in mechanical and biological performance, as evidenced by studies employing plasma electrolysis oxidation and micro-arc oxidation [10-12]. Rafieerad et al. [13] have demonstrated the feasibility of enhancing the adaptability and hardness of Titanium alloy by the inclusion of HA via plasma electrolysis oxidation. Furthermore, the creation of a porous HA surface layer has been associated with augmented bioactivity, a finding corroborated by additional research [13, 14]. Yang et al. [15] reported the formation of a significant apatite layer on HA/Ti composite coatings, suggesting an improvement in bioactivity compared to the uncoated substrate alloy.

FGMs stand apart by exhibiting a continuous transition in properties across their volume, attributable to variations in chemical composition and microstructure. These composites, with their multi-phase microstructure, draw inspiration from natural solutions to engineering quandaries [16]. Developed initially in Japan during the 1980s for aerospace applications, FGMs aimed to alleviate thermal stresses and enhance metal-ceramic adhesion in rocket engines [17]. Today, their utility spans diverse sectors including aerospace, automotive, electronics, defense, and beyond, marking them as a relatively nascent material class [18].

Advancements in composite material technology have led to the development of FGMs with engineered variations in composition and microstructure, designed to improve thermal and mechanical stress resistance. Powder metallurgy, a prevalent technique for FGM creation, involves the meticulous blending of powders, compaction, and sintering, resulting in a material with a stepwise variation in properties, whereas centrifugal methods can achieve a continuous gradient [19].

In the current research, the design, fabrication, and characterization of multi-layered NiTi(HA) FGMs are presented. Employing powder metallurgy, samples comprising three and five layers were synthesized, transitioning from NiTi-rich to HA-rich ends. These specimens were subjected to a uniform compression of 450 MPa and sintered at 1000°C for a period of three hours, parameters that were carefully optimized for the material's integrity and functional gradient.

2. EXPERIMENTAL PART

2.1 Starting materials

This study utilized elemental powders, including Ni, Ti, and HA, to create various FGM layers. Table 1 displays the mean particle size and origin of these powders.

Table 1. Powders utilized in the present research

Powders	Mean Particle Size (μm)	Origin
Nickel	58.41	BDH Chemicals Ltd Poole England
Titanium	4.912	Fluke Chemi AGCH-9470 Bucks
Hydroxyapatite	1.088	Prepared eggshell-derived

Titanium and nickel powders were chosen because titanium and nickel (TiNi) alloys have emerged as potential orthopedic implant materials due to their high corrosion resistance, high specific strength, low modulus of elasticity, superelasticity, and high microhardness. Hydroxyapatite was also chosen because it has excellent biocompatibility and is a biologically active material. Hydroxyapatite constitutes about 70% of the weight of natural human bone

2.2 Plan of work

The work plan outlined can be described as follows:

i. Creating FGM layers based on the predetermined model profile, as Tables 2 and 3 specified.

Table 2. Model of FGM_1 profile

Layers	Chemical Analysis (%)	Thickness (mm)
1st	100HA	3
2nd	50NiTi-50HA	2
3rd	50NiTi50	1

Table 3. Model of FGM_2 profile

Layers	Chemical Analysis (%)	Thickness (mm)
1st	100HA	3
2nd	25NiTi-75HA	2.5
3rd	50NiTi-50HA	2
4th	75NiTi-25HA	1.5
5th	50NiTi50	1

ii. The powders were mixed in a wet state for 7 hours by using planetary automatic ball mill and five steel balls differ in diameter.

iii. The powders were filled into the die cavity in a controlled, step-by-step manner.

iv. The powders were compacted under pressure 450Mpa, the layers were pressed by using an electric hydraulic press type (compacting machine type, made in the U.S.A).

v. All produced specimens were sintered in a vacuum furnace using argon as an inert gas.

The following procedure was followed illustrated in Figure 1.

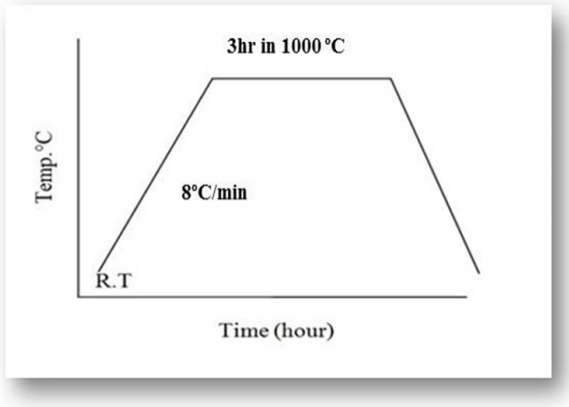

Figure 1. Sintering cycle representation

Since the inter-diffusion between Ti and Ni is enhanced at the sintering temperature (1000°C), which was approximately 0.8 of the melting temperature of the NiTi intermetallic compound (Tm = 1310°C), maintaining that temperature for three hours under a controlled argon atmosphere will result in a complete sintering reaction and an increase in the amount of NiTi phase produced [20].

i. Green and apparent density, as well as porosity, were measured.

ii. Hardness tests were performed individually on each layer of the produced specimens to analyse the property gradation throughout the thickness.

2.3 Compositional graded formula and design of FGM

They are many models used to the estimate volume of friction of FGMs constituents. In this work model that is used after Markworth et al. [21]:

$$V_1(Z) = \left(\frac{Z_2 - Z}{Z_2 - Z_1}\right)^N \quad (1)$$

$$V_2(Z) = 1 - V_1(z) \quad (2)$$

where:

$V_1(z)$ is the local volume fraction of phase 1, and $V_2(z)$ is the volume fraction of phase 2.

(Z_1) and (Z_2) are pure phase 1 and phase 2 border regions, respectively.

Z is the separation between layer 1 and layer 5, while N is a configurable parameter. Which determines V_1's curvature based on its magnitude (z). Figure 2 shows this function for a subset of values of (N). Assuming that the power law index (N) equals (1) estimate of the volume percentage of each layer, it is evident that by appropriately choosing (N), It is possible to make the curvature more or less concave in both directions [22]. As a result, the weights of the two elements (Ti and Ni powders) in each layer are estimated using the formula below [20].

$$W = \rho \times v \times v_f \quad (3)$$

W stands for weight (g), ρ for material density (g/cm³), V for layer volume (cm³), and vf for volume fraction.

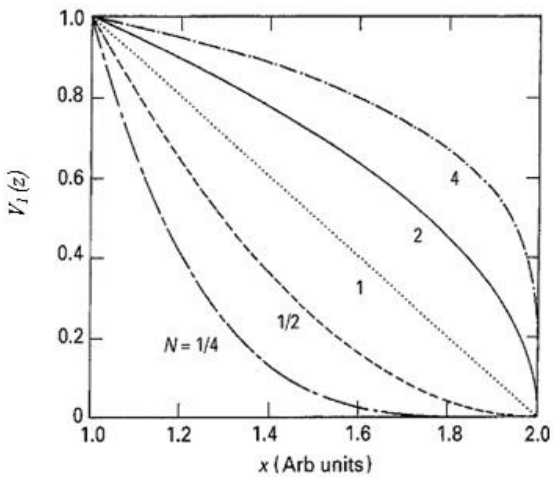

Figure 2. Plot of V1(z) VS Z (Eq. (1)) for selected values of N [22]

The FGM_1 samples comprise three layers: a 3mm-thick Hydroxyapatite layer, a 2mm-thick layer consisting of 50% NiTi and 50% HA, and a 1mm-thick NiTi layer. FGM_2 samples have five layers: a 3mm-thick Hydroxyapatite layer, a 2.5mm-thick layer with 25% NiTi and 75% HA, a 2mm-thick layer with 50% NiTi and 50% HA, a 1.5mm-thick layer with 75% NiTi and 25% HA, and a 1mm-thick NiTi layer. Figure 3 provides a schematic representation of the FGM_1 and FGM_2 samples utilized in this study.

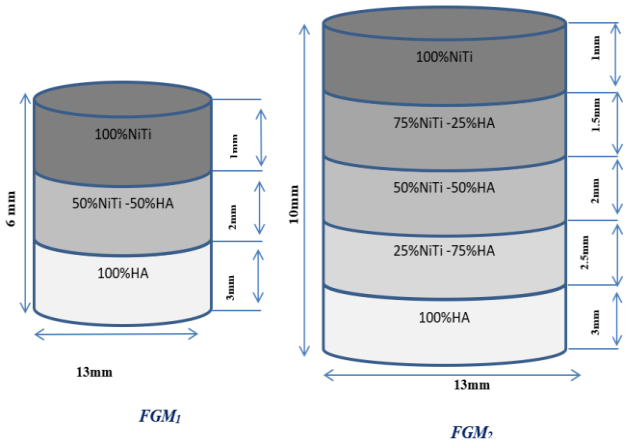

Figure 3. A schematic demonstrates the dimensions of each layer of FGM_1 and FGM_2 samples

After the sintering process, the samples were put through mechanical tests, including micro-Vickers tests and density and porosity to examine the mechanical characteristics and outcomes of adding hydroxyapatite to titanium nickel or the opposite. The examples were made with a 13 mm diameter and a 10 mm height. The FGM samples were divided in half, as demonstrated in Figure 4, to prepare them for hardness testing and FE-SEM analysis

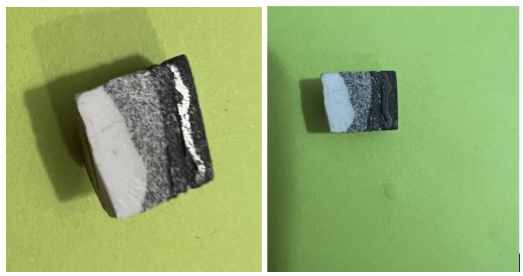

Figure 4. Demonstrates the cutting of the FGM sample

3. DENSITY AND POROSITY

3.1 Apparent powder density of powders and blended

Apparent density is determined by pouring the powder into a standard graduated cup with a maximum volume of 10 ml at the appropriate grade. Care must be exercised to prevent physical densification of the powder in the cup when leveling. A microbalance with an accuracy of 0.001 grams is used to calculate the weight of the cup with and without powder. The next equation gives the apparent density in grams per cubic centimeter [23].

$$\rho_A = \frac{m_2 - m_1}{Vp} \quad (4)$$

where:

ρ_A= Apparent density of powder (g/ cm³).

m_1= weight of cup without powder (unfilled cup) (g).

m_2= weight of cup with powder (g).

Vp = volume of powder in cup (cm³).

3.2 Green porosity and density

The weight in grams per cubic centimeter of a compacted blended powder unit volume. It is the compressed sample's green density. It is computed as follows [23] using compact sample weighting and dimension evaluations:

$$\rho_g = \frac{m_g}{v_g} \tag{5}$$

where:

ρ_g= green density (g/ cm^3).
m_g = green mass of the compressed sample (g).
V_g = volume of the compressed sample (cm^3).

Green porosity is determined from the knowledge of the theoretical density of blended powders (mixture) which is calculated by the weight percent of elemental powder multiplied by its theoretical density as follows:

$$\rho_{tB} = \Sigma wt_1 * \rho_1 + wt_2 * \rho_2 + wt_3 * \rho_3 + \cdots + wt_n * \rho_n \tag{6}$$

where:

ρ_{tB} = theoretical density of mixed powder (g/cm^3).
n = The number of elemental powders.
W_t = weight percent (%).
$\rho_{1,2,3,\ldots n}$ = density of elemental powder (g/ cm^3).

As a result, the green porosity is computed using the following equation:

$$P_g = \left(1 - \frac{\rho_g}{\rho_{tB}}\right) \times 100\% \tag{7}$$

where:

P_g = green porosity (percentage).
ρ_g = green density (g/ cm^3).
ρ_{tB} = theoretical density of mixed mixture (g/cm^3).

3.3 Density and porosity of sintered samples

The density and porosity of sintered part are calculated according to ASTM-B 328-96 [23]:

i- The specimen is dried up to 100°C for 24 hours under vacuum then cooled to room temperature. The weight of dry specimen is measured as mass A.

ii- Using an appropriate evacuation pump at room temperature, the pressure was decreased over the submerged specimen in oil with a viscosity of 22 cst at 37°C for a maximum of 7 kPa pressure for 30 minutes.

iii- Weighting the fully impregnated sample in air, the mass was B.

iv- Weight the fully impregnated specimen in water (Mass F)

v- Measuring the temperature to find the density of water at this temperature.

The investigation was conducted at 21°C., and the density of water (Dw) at this temperature was 0.99802g/cm^3 , density (D) is computed according to the following equation:

$$\mathbf{D} = \left(\frac{\mathbf{A}}{\mathbf{B-F}}\right) * \mathbf{D_W} \tag{8}$$

and a method for measuring porosity is

$$\mathbf{P} = \left[\frac{\mathbf{B-A}}{\mathbf{(B-F)*D^\circ}}\right] * \mathbf{D_w} \tag{9}$$

where, Do = density of oil g/cm^3 =0.963 g/cm^3

4. RESULTS AND DISCUSSION

The experimental data are presented in this study in a sequential manner for discussion. A few mechanical and physical characteristics, including as apparent density, apparent porosity, and particle size analysis both before and after sintering, are included in the experimental results. The microhardness of every FGM layer is one of the mechanical qualities, however. XRD is one method used for the metallurgical characterisation of sintered FGMS and FGMs layers. This study first assessed the physical characteristics of elemental powders, including apparent density, particle size, and particle distribution. In order to prevent any unclear result arrangement, it has been determined that all experimental findings are categorized into before and after sintering.

4.1 Before sintering results of the compacts

In this section, numerous physical test results and various parameters have been examined and presented as follows:

4.1.1 Size and dispersion of particles

Using a particle size analysis, this study examined the particle size and distribution of individual and combined powders (Ni, Ti, and HA). Cumulative plots for each element can be found in Figures 5-7. The mean particle size for each elemental powder is provided in Table 4. Typically, a decrease in particle size reduces apparent density because smaller particles have a larger specific surface area. This increased surface area increases friction between particles, lowering the apparent density [24].

Table 4. Determination of mean particle size for metal powders and mixed blends

Item	Material	Mean Particle Size (µm)
Nickel	Ni	58.41
Titanium	Ti	4.912
HA	$Ca_{10}(PO_4)_6(OH)_2$	1.088

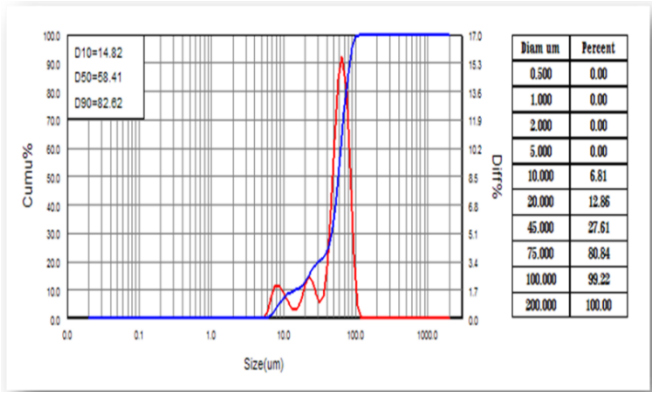

Figure 5. Particle size analysis of Nickel

Conversely, many powders utilized in compaction processes possess irregular shapes. Including fine spherical powders, like Ni powder, can effectively enhance the apparent density. Nevertheless, adding powders in the form of flakes usually results in a decrease in perceived density [25]. The ratio of particles between the coarsest and finest particles, as

well as their respective quantities, influence the perceived density. For the final sintered goods to have the best compacts and desired qualities, specific particle size ranges are selected [24].

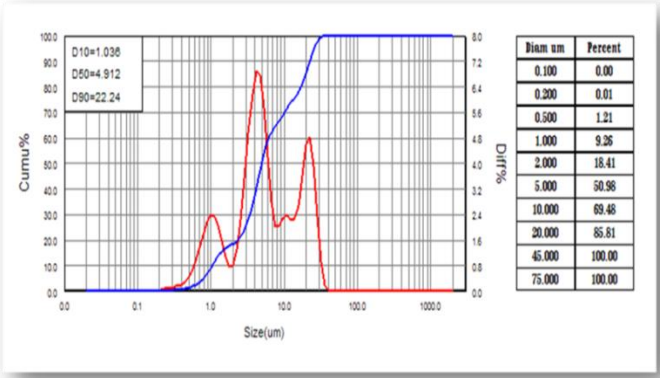

Diam um	Percent
0.100	0.00
0.200	0.01
0.500	1.21
1.000	9.26
2.000	18.41
5.000	50.98
10.000	69.48
20.000	85.81
45.000	100.00
75.000	100.00

Figure 6. Particle size analysis of Titanium

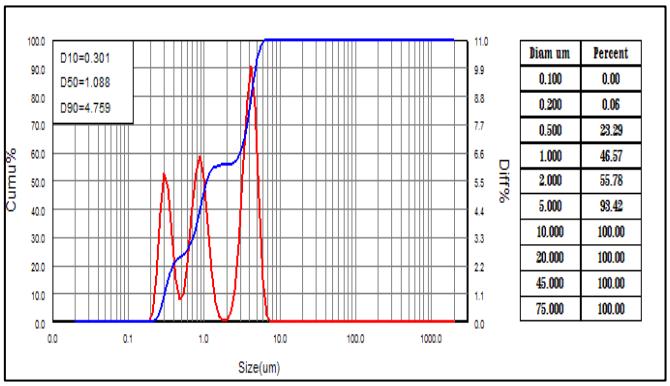

Diam um	Percent
0.100	0.00
0.200	0.06
0.500	23.29
1.000	46.57
2.000	55.78
5.000	93.42
10.000	100.00
20.000	100.00
45.000	100.00
75.000	100.00

Figure 7. Particle size analysis of HAP from eggshells

4.2 Evaluation of apparent density for pure and combined powder mixtures

The apparent density of the elemental powders used to create mixed alloy compositions is shown in Figure 8. After titanium and hydroxyapatite, nickel has the third-highest apparent density among the three elements.

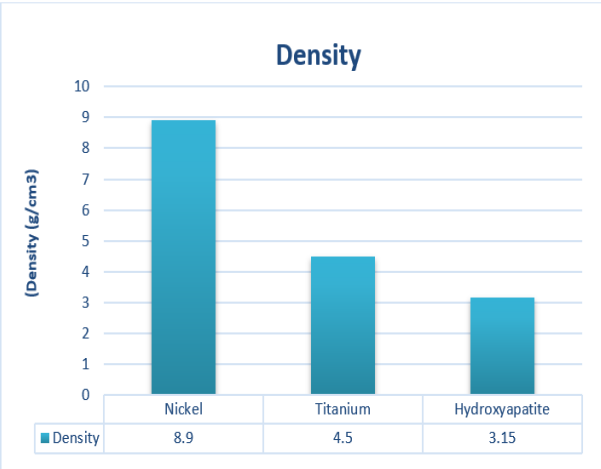

Figure 8. Apparent density for Ti and Ni and hydroxyapatite powders

Particle form, size and distribution, material density, and open spaces within the microstructure all affect the apparent density of metal powders. Particle size and distribution considerably impact apparent density, as fewer spherical particle shapes lead to lower apparent density due to increased surface friction area and reduced uniformity during compaction. The apparent densities of mixed powder combinations for layers 1 to 5 are shown in Figure 9.

Out of all the combinations, the first layer alloy mixture has the highest apparent density due to its larger concentration of denser solid nickel. The apparent densities of mixed and elemental powders are affected by various factors, including:

i. Loading rate and internal friction between particles with similar or different compositions.

ii. Friction resulting from the particles, the narrow funnel, and the baffle box's sidewalls.

As particles more successfully fill the spaces between previously settled particles, decreasing the surface area-to-volume ratio and surface roughness reduces the frictional forces between settling particles and increases apparent density. One useful tactic for increasing the apparent density of pure or mixed powders is to use smaller particles to fill the crevices between bigger ones.

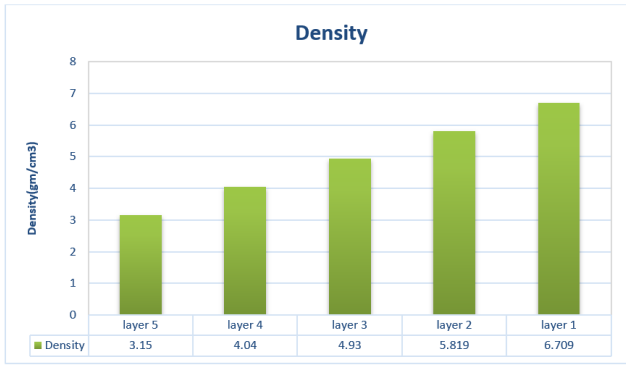

Figure 9. The apparent density of each layer

4.3 The green density of compacts

Based on previous research, six loading rates (300,375,450,525,600 and 675 Mpa) have been considered to explain the impact of the loading rate on the green density of compacts and to select the proper pressure. The impact of the loading rate on the composition of the third layer's green density is depicted in Figure 10. A rise in compacting pressures caused the green density to rise. Then, at pressures of at least 450 Mpa, it is stable. As a result, the samples in this work were compressed at a pressure of 450. Table 5 shows the loading rate values with the corresponding green density values.

Table 5. Green density

Density	Force (Ton)	Pressure (Mpa)
2.6	4	300
2.7	5	375
2.8	6	450
2.8	7	525
2.8	8	600
2.8	9	675

It has been demonstrated that increasing loading rates raise the green density for low-rate loadings, which helps to explain how the rate of loading affects the green density of compacts.

The best sample density is reached after that, when the green density starts to settle and allows us to generate samples with fewer flaws and cracks after sintering. There is a time when the powder particles slide and move together, filling a large number of pores with tiny particles. Additionally, because there is enough time for the gases to escape, the majority of the gases are eliminated from the compact under the action of tension. Moreover, increasing applied stress and time are necessary for any motion of powder particles, just as diffusion depends on temperature, time, and activation energy, which is a function of stress.

Figure 11 shows the relationship between green density and green porosity as a function of compacting pressure. The density of the powder mass increases with increasing compacting pressure because the mass's total porosity decreases. However, it's important to remember that this will also cause changes in pore size and distribution [1].

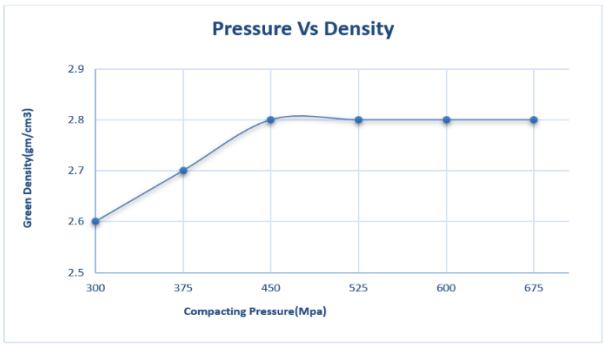

Figure 10. Impact of compacting pressure on the green density of the produced specimen

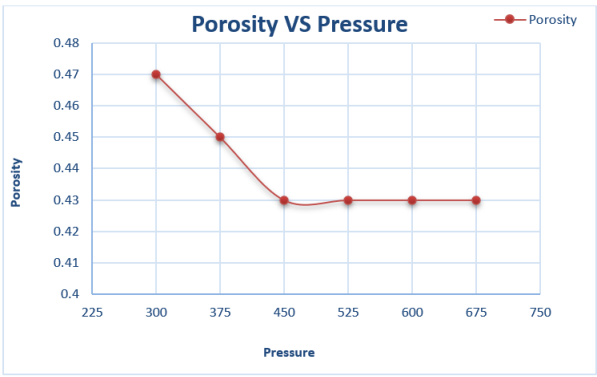

Figure 11. Green porosity concerning compression force

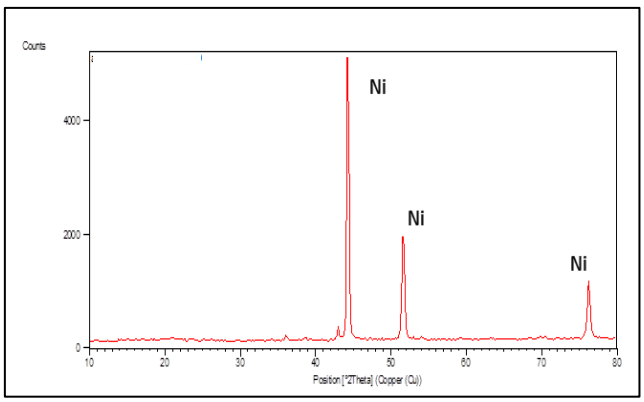

Figure 12. XRD pattern of Nickel powder

4.4 Compacts' X-ray diffraction pattern

The identification of metal powders employed in this study has been explored by X-ray diffraction examinations of powdered titanium and nickel. as illustrated in Figures 12-14. The phases visible in X-ray diffraction examination confirmed the identity of the materials used in this work.

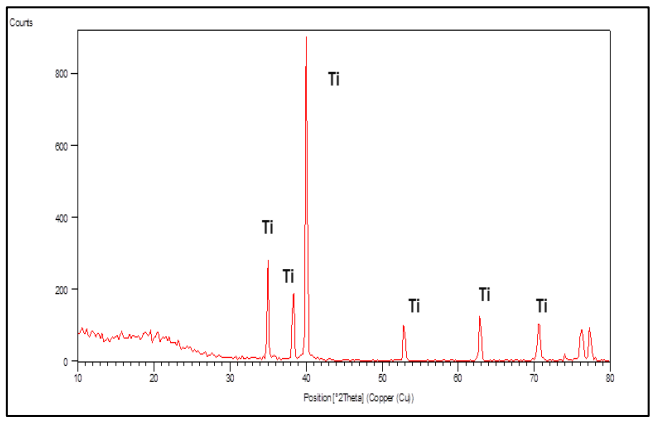

Figure 13. XRD pattern of Titanium powder

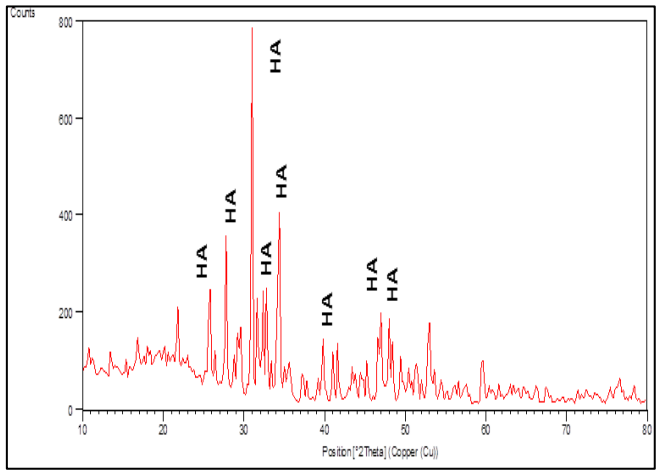

Figure 14. XRD spectrum for the resulting HAP of eggshells

5. RESULTS AFTER SINTERING OF COMPACTS

5.1 Density and porosity after sintering

Sintering techniques greatly affect physical and mechanical features, especially porosity and apparent density. Compacts subjected to higher compacting pressure during sintering generally exhibit fewer pores than those exposed to lower compacting pressure, resulting in an increased apparent density. Figure 15 illustrates the apparent density of the Functionally Graded Material (FGM).

Porosity is the inverse of apparent density, and the temperature and duration of the sintering process primarily influence the shape of pores. Figure 16 presents the porosity levels after the sintering process. Compared to Figure 9, it is clear that porosity decreases post-sintering compared to pre-sintering levels. This reduction occurs because particle diffusion occurs during the sintering process, leading to a reduction in voids and an increase the contacting points between particles.

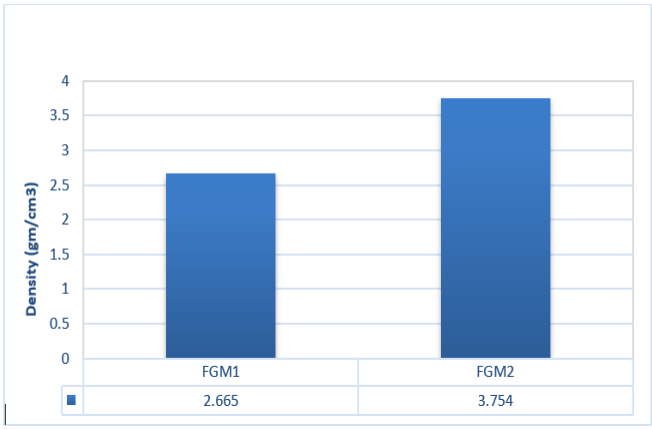

Figure 15. Density of FGM sintered specimen

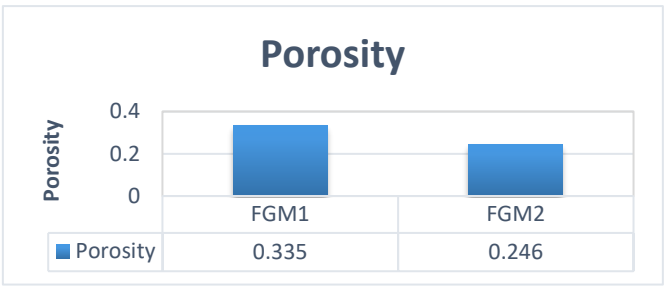

Figure 16. Porosity of FGM sintered sample

5.2 X-Ray diffraction patterns

After exposure to a controlled argon atmosphere and sintered at 1000 degree centigrade for 3 hours, the functionally graded samples were subjected to XRD analysis. A Cu target was utilized in the X-ray tube, resulting in the utilization of λcu = 1.542 °A for obtaining the XRD patterns. The X-ray diffraction (XRD) pattern of the specimens produced is illustrated in Figure 17, indicating the complete conversion of both nickel (Ni) and titanium (Ti) into the monoclinic phase of NiTi, the cubic phase of NiTi, and the hexagonal phase of Ni_3Ti. The occurrence of Ni_3Ti could potentially be attributed to the gradual cooling process of the specimens within the furnace [26]. The proposed reactions throughout the process can be found in the study [27].

$$Ni+Ti \rightarrow NiTi \qquad \Delta G:-67KJ/mol \qquad (10)$$

$$Ni + Ti \rightarrow Ni_3Ti \quad \Delta G: -140\ KJ / mol \qquad (11)$$

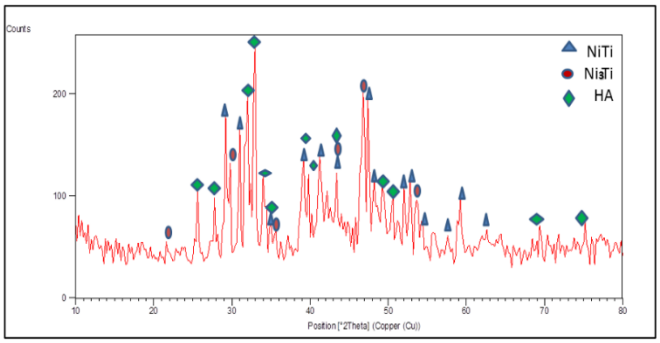

Figure 17. Demonstrates the XRD pattern of FGM

The prepared samples' XRD pattern figure indicates that they are a mixture of two phases—martensitic and austenitic, with a greater proportion of the martensitic phase than the austenitic phase. This suggests that our technique was successful in producing the appropriate specimens and that the prepared samples are made up of both phases.

5.3 Measurements of the hardness

In this investigation, a Vickers microhardness tester of the Digital Screen microhardness tester type Hv-1000 was utilized. With a conventional 136° Vickers diamond pyramid indenter and 20 seconds of holding time on the specimen's surface, this apparatus was used to evaluate the hardness. Optical microscopy was also utilized to quantify the diagonal length of the Vicker's impression. For every layer sample, the three readings are rearranged, and for functionally graded samples, ten readings are collected.

The study conducted hardness tests in order to examine the impact of titanium-nickel on the hardness of pure hydroxyapatite, as well as the reciprocal effect of hydroxyapatite on the hardness of titanium-nickel. Additionally, the objective was to assess the hardness of each individual layer. Microhardness measurements were performed on specimens fabricated using the powder metallurgy technique, which encompassed the processes of compaction and sintering. A mean of five readings was taken at each point to ensure accuracy. The results were illustrated graphically in Figures 18-21.

Since the sample contains both austenitic and martensitic phases, it can be inferred (based on the hardness values) that there is a greater proportion of the martensitic phase than the austenitic phase. It is well known that austenite is stronger and harder in this system than martensite. Consequently,

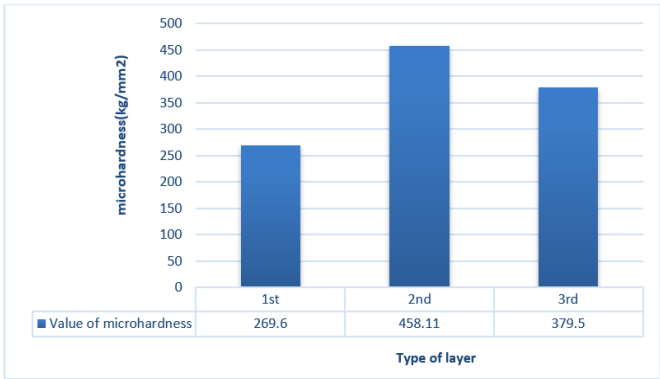

Figure 18. The microhardness of samples with different layers composition

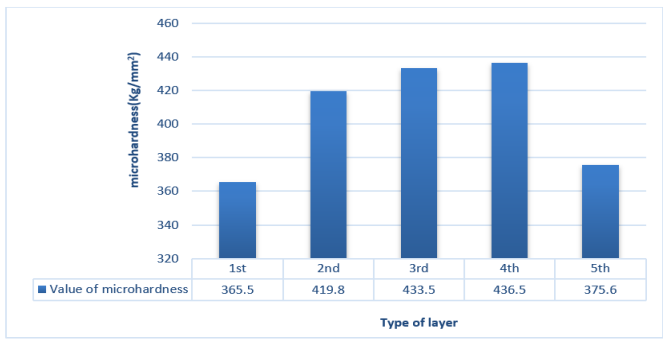

Figure 19. The microhardness of samples with different layers composition

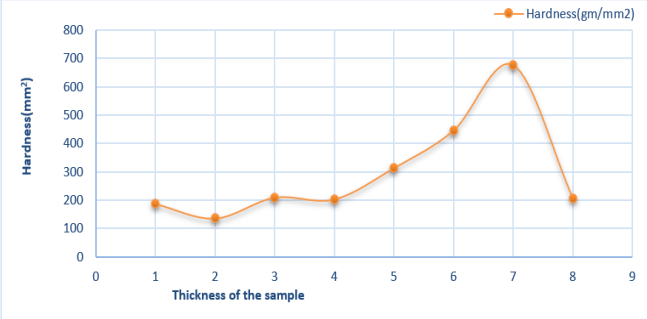

Figure 20. The microhardness of FGM_1 samples with thickness

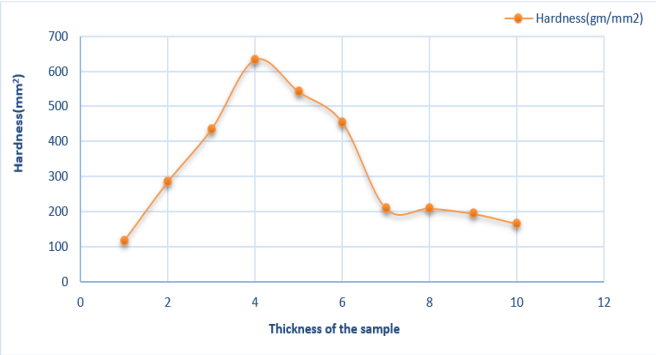

Figure 21. The microhardness of FGM_2 samples with thickness

It is also possible to conclude that a phase having just martensitic properties would be rated as having a lesser hardness. Because of this, the samples are thought to be more ductile and softer than the pure austenitic sample, which is thought to be stronger. This is in line with their respective properties, which are as follows: the thermal material is somewhat flexible, pliable at room temperature, and heat-sensitive enough to return to its old shape. The austenitic material is simply very elastic.

The hardness of NiTi (HA) alloys increases with increasing HA content. Then, it gradually decreases with the increase in the percentage of hydroxyapatite. This is due to the gradation of the layers, where the layers containing only hydroxyapatite or titanium nickel in equal proportions have low hardness values that gradually increase towards the center of the sample containing titanium nickel and hydroxyapatite together. This is consistent with the results of previous studies [22, 27].

Gradient porous materials are important in bone implant applications because they allow control over the design of effective mechanical properties by providing the possibility of adding structural gradients in composition, pores and volume. These gradients can be engineered to reduce internal surface area; In order to facilitate cell adhesion and control these gradients, the structure of the material is designed to match the hardness of bone. The effect of protection from the pressure created at the implant site, which may lead to bone resorption, is a key concern resulting from the mismatch in hardness between the implant and the bone. Consequently, the surgery needs to be reevaluated. Experimental evidence has shown that bone cells can fill cavities in porous implants, affecting the mechanical behavior of the implant, The emerging bone supports the implant structure above the cancellous bone area, thus increasing its rigidity and highly effective resistance to pressure.

6. CONCLUSIONS

The present investigation's findings led to the following conclusions:

- A functionally graded material has been developed that may serve as a replacement for lost or broken bones due to the high number of accidents, bone-affecting deformities, and the challenges associated with treating the injured. The possibility of preparing these materials with good mechanical and physical properties according to standard specifications to replace damaged parts of the bones, and this purpose has been achieved.
- Nickel Titanium alloy (NiTi) in the form of hydroxyapatite (HA) was effectively produced using the powder metallurgy technique and subsequently sintered at a temperature of 1000 degrees Celsius.
- The proposal put forth an axisymmetric design for functionally graded materials consisting of three and five layers, with the aim of achieving a linear variation of constituents, specifically NiTi and HA, across these layers. The performance of functionally graded materials with an axisymmetric design is superior to that of one-directional functionally graded materials or isotropic homogenous materials. One possible substitute for the one-directional functionally graded material is two-directional functionally graded material. Furthermore, two-directional functionally graded materials actually allow for the integrated design of structures and materials.
- The conducted sintering process, carried out at a temperature of 1000 degrees Celsius for a duration of 3 hours, appears to be highly efficient in achieving full sintering and facilitating the conversion of nickel (Ni) and titanium (Ti) into a homogeneous alloy structure.
- Two fabricated models were utilized to demonstrate the presence of a linear variation in chemical composition and microhardness magnitudes along the thickness. With increasing HA content, A distinct increase to a peak value and subsequent fall in microhardness are evident, and these changes are caused by a combination of factors including grain size and phase proportion. 50% of the maximum hardness with HA concentration. But because of the HA volume fraction, the top portion has the maximum ductility.

7. RECOMMENDATIONS FOR FUTURE WORK

- Analyzing corrosion rate using the weight loss method and examining corrosion behavior in the presence of aeration.
- Researching how cycling loading affects the fatigue phenomenon and the shape memory effect.
- Analyzing wear behavior and the impact of heat cycling on the shape memory effect.
- In an effort to remove Ni_3Ti, quench the samples after they have sinterred (after cooling to a specific temperature in the furnace).
- Researching how NiTi's surface characteristics are affected by sterilization.
- The structure, form, and degree of ordering of martensite should be revealed using a transmission electron microscope or high resolution scanning electron microscope.

REFERENCES

[1] Arifin, A., Sulong, A.B., Muhamad, N., Syarif, J., Ramli, M.I. (2014). Material processing of hydroxyapatite and titanium alloy (HA/Ti) composite as implant materials using powder metallurgy: A review. Materials & Design, 55: 165-175. https://doi.org/10.1016/j.matdes.2013.09.045

[2] Li, Y., Yang, C., Zhao, H., Qu, S., Li, X., Li, Y. (2014). New developments of Ti-based alloys for biomedical applications. Materials, 7(3): 1709-1800. https://doi.org/10.3390/ma7031709

[3] Tjong, S.C. (2013). Recent progress in the development and properties of novel metal matrix nanocomposites reinforced with carbon nanotubes and graphene nanosheets. Materials Science and Engineering: R: Reports, 74(10): 281-350. https://doi.org/10.1016/j.mser.2013.08.001

[4] Nemat-Alla, M.M., Ata, M.H., Bayoumi, M.R., Khair-Eldeen, W. (2011). Powder metallurgical fabrication and microstructural investigations of aluminum/steel functionally graded material. Materials Sciences and Applications, 2(12): 1708-1718. https://doi.org/10.4236/msa.2011.2128

[5] Zhu, J., Lai, Z., Yin, Z., Jeon, J., Lee, S. (2001). Fabrication of ZrO_2–NiCr functionally graded material by powder metallurgy. Materials chemistry and physics, 68(1-3): 130-135. https://doi.org/10.1016/S0254-0584(00)00355-2

[6] Kieback, B., Neubrand, A., Riedel, H. (2003). Processing techniques for functionally graded materials. Materials Science and Engineering: A, 362(1-2): 81-106. https://doi.org/10.1016/S0921-5093(03)00578-1

[7] M, S., Sheikh, M.Y., Khan, N., Kurbet, R., Gowda, T.M.D. (2021). A review on application of shape memory alloys. International Journal of Recent Technology and Engineering, 9(6): 111-120. https://doi.org/10.35940/ijrte.F5438.039621

[8] Han, C., Wang, Q., Song, B., Li, W., Wei, Q., Wen, S., Liu, J., Shi, Y. (2017). Microstructure and property evolutions of titanium/nano-hydroxyapatite composites in-situ prepared by selective laser melting. Journal of the Mechanical Behavior of Biomedical Materials, 71: 85-94. https://doi.org/10.1016/j.jmbbm.2017.02.021

[9] Zhang, L., He, Z.Y., Zhang, Y.Q., Jiang, Y.H., Zhou, R. (2016). Enhanced in vitro bioactivity of porous NiTi–HA composites with interconnected pore characteristics prepared by spark plasma sintering. Materials & Design, 101: 170-180. https://doi.org/10.1016/j.matdes.2016.03.128

[10] Bovand, D., Yousefpour, M., Rasouli, S., Bagherifard, S., Bovand, N., Tamayol, A. (2015). Characterization of Ti-HA composite fabricated by mechanical alloying. Materials & Design (1980-2015), 65: 447-453. https://doi.org/10.1016/j.matdes.2014.09.021

[11] Durdu, S., Usta, M. (2014). The tribological properties of bioceramic coatings produced on Ti6Al4V alloy by plasma electrolytic oxidation. Ceramics International, 40(2): 3627-3635. https://doi.org/10.1016/j.ceramint.2013.09.062

[12] Chang, Q., Ru, H.Q., Chen, D.L., Yang, J.L., Hu, S.L. (2014). Effect of iron on the sinterability and properties of HA/Ti-Fe composites. Advanced Materials Research, 898: 271-274. https://doi.org/10.4028/www.scientific.net/AMR.898.271

[13] Rafieerad, A.R., Ashra, M.R., Mahmoodian, R., Bushroa, A.R. (2015). Surface characterization and corrosion behavior of calcium phosphate-base composite layer on titanium and its alloys via plasma electrolytic oxidation: A review paper. Materials Science and Engineering: C, 57: 397-413. https://doi.org/10.1016/j.msec.2015.07.058

[14] Lugovskoy, A., Lugovskoy, S. (2014). Production of hydroxyapatite layers on the plasma electrolytically oxidized surface of titanium alloys. Materials Science and Engineering: C, 43: 527-532. https://doi.org/10.1016/j.msec.2014.07.030

[15] Yang, S., Li, W.H., Man, H.C. (2013). Laser cladding of HA/Ti composite coating on NiTi alloy. Surface Engineering, 29(6): 409-431. https://doi.org/10.1179/1743294413Y.0000000115

[16] Al-Shafaie, S.H., Nabaa, S.R., Hussein, M.A. (2021). Preparation and investigation mechanical properties of functionally graded materials of Aluminum-Nickel alloys. Journal of Mechanical Engineering Research and Developments, 44(4): 102-109.

[17] Chauhan, P.K., Khan, S. (2020). Microstructural examination of aluminium-copper functionally graded material developed by powder metallurgy route. Materials Today: Proceedings, 25: 833-837. https://doi.org/10.1016/j.matpr.2019.10.007

[18] Kayabasi, I., Sur, G., Gokkaya, H., Sun, Y. (2022). Functionally graded material production and characterization using the vertical separator molding technique and the powder metallurgy method. Engineering, Technology & Applied Science Research, 12(4): 8785-8790. https://doi.org/10.48084/etasr.5025

[19] Dawood, N.M. (2014). Preparation & characterization of coated & cu alloyed bio nitinol. Doctoral dissertation, Ph. D. Thesis, University of technology. Fabricated from Special Thermo mechanically Processed NiTi Wire, Ph. D. Thesis, Ohio State University.

[20] Radhi, N.S. (2015). Preparation, characterization, and modeling functionally graded materials in bio-application. Doctoral dissertation, PhD thesis. University of Technology. Iraq.

[21] Markworth, A.J., Ramesh, K.S., Parks, W.P. (1995). Modelling studies applied to functionally graded materials. Journal of Materials Science, 30: 2183-2193. https://doi.org/10.1007/BF01184560

[22] Khafaji, N.S.L., Hafiz, M.H., Atiyah, A.A. (2018). Sintering of incorporated shape memory alloys into functionally graded materials. Industrial Engineering & Management, 3: 2169-0316. 10.4172/2169-0316.S3-002

[23] ASTM, B. (2003). 328" Standard Test Method for Density. Relative density (Specific Gravity), and absorption of fine aggregate.

[24] Raheem, A., Abid-Ali, K. (2008). Investigation of certain shape memory alloys in space systems. Ph.D thesis, Dep. Mater. Eng. Eng. Univ. Babylon–Iraq.

[25] Meng, Q. (2012). Functionally graded NiTi materials. PhD. thesis, West. Univ.

[26] Goryczka, T., Van Humbeeck, J. (2006). Characterization of a NiTiCu shape memory alloy produced by powder technology. Journal of Achievements in Materials and Manufacturing Engineering, 17(1-2): 65-68.

[27] Wang, J., Pan, Z., Ma, Y., Lu, Y., Shen, C., Cuiuri, D.,

Li, H. (2018). Characterization of wire arc additively manufactured titanium aluminide functionally graded material: Microstructure, mechanical properties and oxidation behaviour. Materials Science and Engineering: A, 734: 110-119. https://doi.org/10.1016/j.msea.2018.07.097